Single-Component Average Velocity Profiles in the Wake of the Orion Crew Capsule at the National Transonic Facility

Jonathan E. Retter[1] and Olivia Tyrrell[2]
National Institute of Aerospace, Hampton, VA, 23666, United States

Bryce Moran[3], James Montgomery[4], and Bill Dressler[5]
Jacobs Technology, Inc., Hampton, VA, 23666, United States

Karen L. Bibb[6], Gregory J. Brauckmann[7], Daniel T. Reese[8] and Paul M. Danehy[9]
NASA Langley Research Center, Hampton, VA, 23681, United States

A minimally intrusive molecular tagging instrument measured single-component average velocity profiles in two planes in the wake of the Orion capsule with different heat shield configurations in the National Transonic Facility at the NASA Langley Research Center. Reynolds number effects at subsonic conditions have proven difficult to predict due to the largely separated wake flow. Therefore two measurement planes in the wake of the model were probed to measure the wake profile for different heat shield configurations and act as a validation reference for computational tools. Air testing included Mach numbers of 0.3, 0.5, and 0.7 at Reynolds numbers of 5.3 and 7.5 million. In cryogenic nitrogen, the instrument was employed under transient conditions during the facility warm up at M = 0.3 with decreasing Reynolds numbers from 16 million. An exhaustive list of the results is shown and discussed here. For free transition heat shield configurations, the size of the wake was found to increase with Mach number, yet remain constant with Reynolds number for low (M = 0.3) and high (M = 0.7) subsonic Mach numbers. However, intermediate Mach numbers (M = 0.5) showed that the wake was smaller at higher Reynolds numbers for the IDAT heat shield. The addition of surface roughness in the form of grit, known as the fixed transition cases, negated any Mach number dependence to the wake profile and increased the size of the wake for all cases.

I. Introduction

The NASA Orion capsule, formerly known as the Crew Exploration Vehicle (CEV) [1], is the Apollo-inspired Space Shuttle replacement tasked with transporting humans and cargo to low Earth orbit, the moon, and Mars aboard the Space Launch System (SLS) during the Artemis Missions. While similar in major design features to the Apollo Command Module to decrease the development time (spherical blunt body with a heat shield and conical back shell), Orion is a physically larger vehicle with over 2.5 times the volume of the Apollo module [2]. The development of Apollo-era spacecraft was before the advent of CFD and therefore relied heavily on experimental ground testing in

[1] Research Engineer
[2] Research Engineer
[3] Test Engineer
[4] Instrumentation Specialist
[5] Instrumentation Specialist
[6] Aerospace Engineer
[7] Aerospace Engineer
[8] Research Engineer
[9] Senior Technologist

wind tunnel facilities with validation from flight test data [3]. In contrast, CFD guided the design of Orion with sparser wind tunnel tests aimed throughout the development cycle to validate the predictive models [4]. While computational models are improving over time and replacing the need for costly experiments, CFD remains unreliable in some instances such as smooth-body flow separation. CFD can sometimes predict the correct wind tunnel force and moment data, while inaccurately predicting the off-body flowfield. Therefore, ground testing of flight vehicles, particularly with advanced measurement capabilities focused on measuring more fundamental flow properties, remain a critical research step to validate and help reduce uncertainties in these prediction codes of the vehicle behavior.

Several such tests on the Orion crew capsule have been performed in a variety of wind tunnel facilities [5,6] and summarized in the aerodynamic database for both the subsonic/supersonic [7] and hypersonic [8] regimes. Force and moment measurements coupled with surface pressures are routine deliverables from wind tunnel facilities and offer the main source of validation data, but advanced diagnostic capabilities have recently offered more detailed comparisons. On-body techniques such as temperature-sensitive paint (TSP) and infrared (IR) imaging have found use in monitoring the boundary layer state on the heat shield in supersonic flow [2] or pressure-sensitive paint (PSP) to monitor the flow separation on the back shell [4], revealing the strong Reynolds number dependency of the vehicle at subsonic Mach numbers. Several studies with sting-free mounting configurations allowed for the study of the vehicle wake to assist with the parachute deployment during subsonic re-entry, including wake rake measurements in subsonic flow [9], shadowgraph measurements in an aeroballistic range [10], and an impressive comprehensive experimental study including particle imaging velocimetry (PIV), PSP, IR imaging, shadowgraph imaging, and boundary layer traversing pressure probe measurements [11] with a coinciding simulation effort [12]. More unique visualization efforts include background oriented schlieren on Orion-like vehicles [13], NO PLIF to visualize reaction control system jets in a Mach 10 flow [14], and IR imaging of the Orion heat shield on an actual re-entry test of the Orion capsule [15].

The focus of this work is to present the results from the recent application of a molecular tagging velocimetry (MTV) instrument to measure wake profiles during the wind tunnel test of a 7% scale model of the Orion Crew Capsule performed in the NASA Langley National Transonic Facility (NTF). As a pressurized cryogenic facility, the 8.2x8.2x25 ft test section of the NTF offers the unique capability of flight-realistic Mach and Reynolds numbers for scaled models [16] but significant challenges for the implementation of laser diagnostics. For this recent Orion test (T233), subsonic to transonic Mach numbers were tested from 5.3 to 28 million flight Reynolds numbers (based on the heat shield diameter, 13.86 inches) to add re-entry data to the aerodynamic database for the vehicle with three different heat shields. This fits a direct need for the Orion aerodynamic database, as the subsonic flight regime is the most difficult to model accurately [12,17] (due to the three dimensional flow separation and corresponding reliance on turbulence models), and subsonic Reynolds number effects on Orion remain unvalidated [7]. A subset of these conditions featured the MTV system denoted Femtosecond Laser Electronic Excitation Tagging, or FLEET. A two-plane wake strategy was applied to all heat shields at a variety of Reynolds numbers for Mach numbers of 0.3, 0.5, and 0.7. The results and brief analysis are presented here. This document, together with the corresponding practical guide focused on the experimental setup and data processing and the text files containing the results examined in this document, offer a summary of the FLEET efforts in the NTF to support the NASA Orion Team.

II. Experimental Setup

A. FLEET System

As such a large, unique facility, the FLEET setup is likewise unique and custom to meet the harsh, cryogenic environment. The details of the system could fill a paper on its own, and indeed it already has. The reader is encouraged to review these works [18,19] for a proper understanding of the components of the system, whereas a broad overview of the single-laser single-detector system is discussed here, revolving around the cartoon experimental setup in Fig. 1

The lasing system is a Spectra Physics Solstice Ace (1 kHz, 7W, 800 nm, 100 fs) located one story above the NTF test section. The beam was delivered into the tunnel and test section by a custom system of motorized mirrors in an evacuated piping system known as the laser penetration system (LPS) to reduce the degradation of the beam over the long path length from the laser to the test section (~80 ft). For the test, the beam was expanded before entering the LPS to reduce white light generation on the windows, allowing the full pulse energy to be used for the test. However, due to the lack of environmental control and duration of the test (April-November 2021), the pulse energy of the system varied greatly from ~5 to 6.7 mJ out of the laser housing, relating to a range of 2.9 to 3.8 mJ as measured on the floor of the test section after the beam focus in ambient air. Final focusing optics and a motorized sweep mirror guided the beam through the top wall of the test section and down towards the model. While the combined -300 mm, +400 mm lens system was stationary and fixed the focal length at ~58 inches away from the downstream lens, the physical position of the FLEET signal and thus measurement volume was adjusted with the sweep mirror. The top

right of Fig. 1 depicts a simplified form of the laser delivery into the test section along with a picture of the FLEET signal next to the model in the test section under atmospheric conditions. Due to the discrete optical access of the facility and geometry of the model, the laser was aimed through the port window at an angle (~14.5° upstream and between 7° and 8° towards the far side wall), diminishing the intensity of the FLEET signal because of the increased distance to focus the laser to the model's location near the tunnel centerline.

The detector system comprised of a Photron Fastcam Mini AX-200 attached to either a LaVision IRO-X and later to an original IRO after a hardware failure with the IRO-X mid-test. Typical IRO settings were 80-85% gain depending on the laser scatter that day off the model and a 5 μs gate to maximize the signal. A Canon 135 mm f/2 lens was remotely controlled with an ISSI EF Lens controller (LC-2). Due to the geometry of the setup, the entire detector system was angled 9.4° upstream in order for the field of view to overlap with the location of the model and FLEET signal. Note that the measured component of velocity is that in the 2D plane perpendicular to the view of the detector, therefore the vector component is not perfectly freestream in this case. The top left of Fig. 1 shows an example detector image of the FLEET signal next to the model rolled to -90° in atmospheric conditions.

A LabVIEW-based acquisition code automated the data acquisition by controlling the laser shutter, camera focus, camera trigger, and position of the final motorized sweep mirror for each point with hopes of measuring the shear layer off the vehicle shoulder. For each physical location, ~222 images were acquired at different detector delays depending on the conditions of the experiment (combinations used include 0, 4, and 8 us, 0, 6, and 12 us, 0 and 4 us, and finally 0 and 3 us). The bottom right of Fig. 1 shows the timing diagram, where the delay of the intensifier exposure changed from one image to the next. The delayed FLEET signal was too weak for single-shot acquisition and required averaging all common delay images across the total number of shots at a particular physical location.

For absolute positioning and safety (to avoid hitting the model), the beam spot on the floor was monitored with a series of a tunnel surveillance cameras. Assuming the position entering the tunnel through the port 8 window in the ceiling is constant (or the variation is negligible), the position next to the model can be inferred just by knowing the position of the beam on the floor. Day-to-day and condition-to-condition shifts in the position of the beam are monitored with this system.

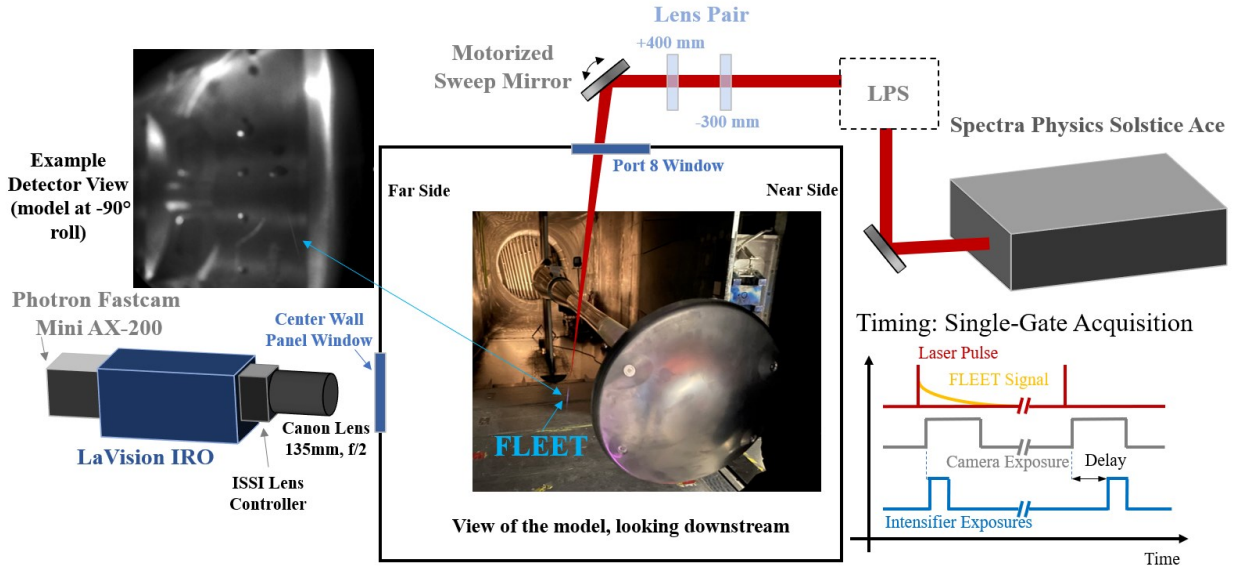

Fig. 1 Cartoon of the experimental setup. The detector system looking through the far side center wall panel window with an example image of the FLEET signal and model are on the left side of the figure. The center shows an image of the FLEET signal next to the model with an Abort heat shield installed in the test section. The top of the figure shows a simplified drawing of the laser delivery into the test section through port window 8. Finally, the timing diagram for the laser, FLEET signal, and detector acquisition is shown in the bottom right side of the image.

B. Model Geometry and Measurement Location

Fig. 2(a-c) presents the three different heat shields tested in a "clean" configuration with no surface roughness ("free" or natural transition), denoted as the (a) Abort, (b) Fenced, and (c) axisymmetric Integrated Design and Analysis Team (IDAT) heat shields. The Abort heat shield is the pre-flight asymmetric geometry, with additional

material added to regions with the highest expected surface heating. The Fenced heat shield is the predicted shape after ablation during re-entry with the maximum predicted fence height. Finally, the IDAT heat shield is a generic axisymmetric shape, nominally representing a pre-flight shape without modifications to counteract the expected heating. Both the Fenced and IDAT shields were also tested with surface roughness ("fixed" transition), depicted on the Fenced heat shield in Fig. 2(d) with the addition of grit on the surface of the heat shield. Both #240 silicon carbide grit and #600 silicon carbide grit were used and are hereby defined as grit and fine grit, respectively. Clean heat shields are representative of flight-abort configurations, where the heat shield boundary layer is expected to be laminar, whereas the grit heat shields offer a representation of actual re-entry flight where some of the surface will burn and degrade leading to a more turbulent boundary layer on the heat shield. Fig. 2(e) depicts an approximate view from the detector location on the far side wall of the time-integrated FLEET signal in atmospheric conditions next to the model at 0° roll. This signal level is typical of what one would see by eye during setup in the test section. Only results from the IDAT testing are presented in this work.

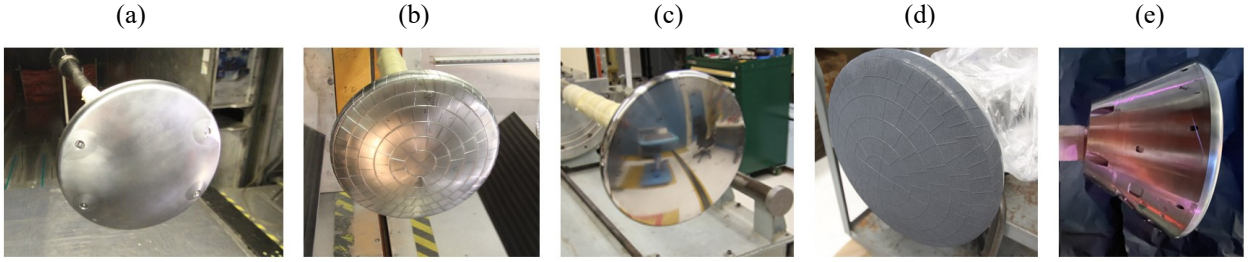

Fig. 2 Heat shields tested throughout the entry: (a) Abort, (b) Fenced, (c) IDAT, (d) an example of a Fenced heatshield with grit (the Fenced and IDAT heat shields were tested with grit, otherwise known as "fixed transition"), and (e) a side view showing the nominal position of the FLEET measurement volume with respect to the model.

After a discussion with the customers and a proper understanding of the limitations of the measurement instrument, a 32-point, 2-plane measurement strategy was adapted as described in Fig. 3(a). The first point of the sweep, point 1, is the closest approach to the model, with the measurement location translating through the shear layer away from the model in the wall-normal direction to point 16, nominally in the freestream. This first plane comprised of points 1 through 16 is denoted the upstream plane and requires ~56 seconds, limited mostly by the slow speed of the sweep mirror repositioning the beam between points (8823-AC Picomotor Piezo Mirror Mount at 2000 steps/sec). There is then a large gap in the measurement sequence (~40 seconds) as the motorized mirror repositions the measurement volume downstream to start the second, or downstream, measurement plane at point 17. The measurement then proceeds back through the shear layer and ends at point 32, before returning home (another ~40 seconds) to point 1 to prepare for the next run. The distance between measurement points on a single plane is 0.112 inches (2.85 mm) and the distance between measurement planes is 1.84 inches (~46.7 mm). The positioning of the points in the measurement sweep is pre-programmed in a LabVIEW code and tested in the test section before the entry by burning holes in a piece of construction paper with the laser on the centerline of the tunnel to ensure the desired sweep pattern. The imaging plane of the detector was rotated 9.4° from parallel to the wall (the exaggerated white line in Fig. 3(a)), accomplished by rotating the entire detection system in order to see the model in the tunnel. The detector focus was adjusted automatically from point-to-point using the lens controller mentioned above.

The model coordinate system is utilized for absolute positioning, with an origin at the vertex of the conical shape produced by the model back shell [6]. For this entry, the model was mounted on the sting with either a 174° or 186° angle, therefore for a model roll of +/-90° the model x-z coordinate plane was rotated 6° from the tunnel frame. Fig. 3(b) depicts this x-z plane with a cross-section of the model at y = 0 inches (vertical tunnel centerline) along with the zero-point, velocity unit vectors, and the measurement planes. Different color profiles describe different model mounting angles to the sting, where the black profile (180°) was never used in the experiment but represents a "tunnel" frame and the rotation required to move the measured planes and velocity vectors onto the model coordinate system. In the tunnel frame, the black measurement planes and velocity vectors depict what the detector measures for all runs. However, for example with the red 174° case, the model must be rotated 6° clockwise about the center of rotation, shifting the measurement planes and velocity unit vectors from the tunnel frame (black lines) to the corrected model frame (red lines). This correction is dependent on the sting angle and the model roll and is applied to all physical dimensions for each measurement case.

The unit vector of the measured velocity changes depending on the model roll and mounting angle to the sting. The velocity unit vector for the 174° sting mounted case in [x,y,z] is [-0.964, 0.000, 0.266] for +90° roll (red vector

in Fig. 3(b)) and [-0.998, 0.000, -0.059] for -90° roll (blue vector in Fig. 3(b)). Therefore, even with the angled imaging plane, both measured conditions are overwhelmingly in the freestream direction but will require knowledge of the z-component from any computations to accurately predict or compare against the measured velocity component. The measurement resolution in the tunnel frame ranged from 0.0063 to 0.0059 inches/pixel (0.16 to 0.15 mm/pixel) in the y-coordinate (vertical, along the measurement line), 0.112 inches (2.85 mm) in the z-axis (the discrete measurement locations towards and away from the model), and 1.84 inches (~46.7 mm) in the x-axis (the relative location of the upstream and downstream planes).

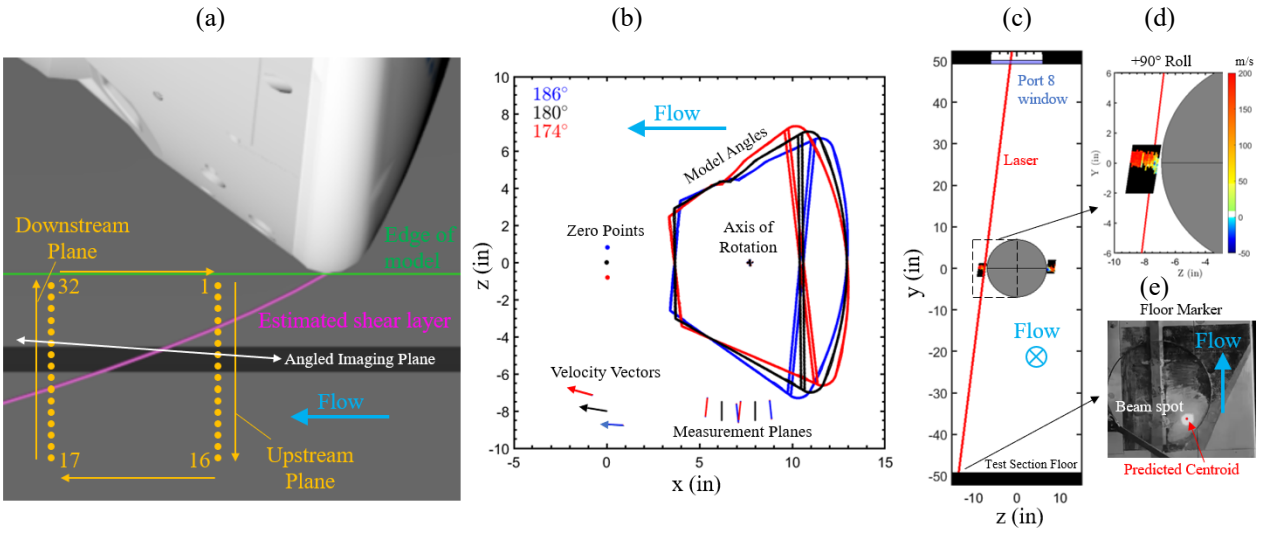

Fig. 3 Description of the FLEET measurement location with respect to the Orion model. (a) Example 32-point, 2-plane sweep pattern overlaid on a CAD drawing of the model rolled to -90° with an estimation of the shear layer position and an example of the angled imaging plane. (b) A 2D slice of the model rolled to +90° in the x-z plane at y = 0 inches to show the model mounted to the sting at 186° (blue), 180° (black), and 174° (red). Each mounting case has corresponding zero points, velocity vectors, and measurement planes corresponding to the rotation about the marked axis. (c) View of the model looking downstream with a typical laser configuration emanating 1.5 inches off center of the tunnel z-axis at a 7° angle. The inserts include (d) a close-up view of the +90° roll measurement plane and (e) an image of the beam spot on the floor marker used to determine the absolute z-axis of the model.

While the motor command settings for the relative positions of the points were constant throughout the test, the absolute positions of the two planes with respect to the model shifted slightly day-to-day due to changing tunnel and environmental conditions. These changes were accounted for with the floor marker monitoring system and defined the starting z-coordinate for all upstream measurement planes (e.g. point 1 from Fig. 3(a)). The absolute positions of the remaining points are set from the known relative commands to the sweep mirror and are assumed constant throughout the test. Fig. 3(c-e) show this process of beam monitoring on the floor, with Fig. 3(c) depicting a view looking downstream of the sting-mounted model rolled to +90° at the center of the test section and the laser originating from the port 8 window ~1.5 inches off the centerline of the tunnel and angled at 7°. The laser is focused on the far side of the model to produce the FLEET signal and expands until it hits the floor. A zoomed view of an example measurement plane is shown in Fig. 3(d), and an image of the floor marker is shown in Fig. 3(e). By imaging the beam spot on the floor and knowing the exit of the laser from the port window, the absolute position of the measurement volume with respect to the model is determined for all sweep patterns though camera failures later in the test increased the uncertainty of some of these absolute position determinations.

C. Experimental Conditions

Table 1 shows the test Mach and Reynolds numbers that featured FLEET in air mode, with the corresponding tunnel conditions required to achieve these conditions shown in Table 2. Due to the inability to adjust the focal length of the laser remotely, the model was held at 0° pitch with roll angles of +90° and -90° with repeat runs available for a few conditions. While this is not an angle of attack the vehicle flies at, it does provide the ability to test the predictive capability of simulation tools and tune turbulence models on the highly separated wake flow of the vehicle. This model/laser orientation was chosen primarily to avoid having the laser hit and damage the model. A full set of 32-point, 2-plane sweeps with repeats were scheduled for each case originally, but combinations of low priority with time

constraints and facility issues prevented FLEET data acquisition for all heat shields and conditions. For the IDAT heat shield, the "filled" designation denoted model filler in the orifices and indented features to "fill" the nominal conical back shell and present a non-ITAR version of the model. This white filler was covered with a black sharpie to mitigate scatter issues from the facility lights and/or the laser scatter itself.

Table 1 Summary of the air data runs for FLEET for each heat shield configuration

		M = 0.3				M = 0.5				M = 0.7			
		Re = 5.3		Re = 7.5		Re = 5.3		Re = 7.5		Re = 5.3		Re = 7.5	
		+90	-90	+90	-90	+90	-90	+90	-90	+90	-90	+90	-90
Abort	Clean	X	X	X	X	X	X	X	X	X	X	X	X
Fenced	Clean			X	X	X	X					X	X
	With Grit	X	X	X	X	X	X	X					
IDAT	Clean, filled	X	X	X	X	X	X	X	X	X	X	X	X
	Clean, not filled	X*	X*	X*	X*	X†	X†	X†	X†				
	Clean, 186 deg, filled			X	X			X	X				
	Grit, 186 deg, filled	X	X	X	X	X	X	X	X	X	X	X	X
	Fine grit, not filled			X	X			X	X				

*Actually M = 0.4
†Actually M = 0.6
Red X = repeat run available

Table 2 Nominal tunnel operating conditions corresponding to the air runs

	M = 0.3		M = 0.5		M = 0.7	
	Re = 5.3	Re = 7.5	Re = 5.3	Re = 7.5	Re = 5.3	Re = 7.5
Total Temperature (°F)	120	120	120	120	120	120
Total Pressure (psia)	37.89	53.59	24.38	34.39	19.245	27.23

For cryogenic nitrogen, measurements were limited to the facility warmup due to (1) the duration of time required to complete a FLEET sweep pattern (3 minutes) was long compared to the typical measurement point in cryogenic operation (~4 seconds), leading to a large use of LN_2, and (2) the inability to reliably focus the laser beam while the facility is cooling down or operating under normal conditions. While the first issue could be eliminated with the implementation of a faster motorized mirror, it is theorized this second issue is due to the injection of LN_2 leading to a stochastic variation in the laser focus with decreasing temperature until the signal disappears. However, the same conditions can be measured during facility warm up that cannot be measured while the facility is cooling down. Therefore, as limited to the facility warm up, the conditions are transient over the ~3 minute measurement window of the 2-plane sweep and the Mach number is limited to 0.3 to prevent the facility from warming up too fast. For example, with a tunnel total temperature near -200° F, the temperature increases by ~15° F over ~3 minutes of run time at M = 0.3, but only increases by ~2° F when the tunnel is near 0° F. An additional, and unfortunate, constraint was the facility warmups typically aligned with an unrelated issue in the facility requiring warmup and eventual repairs. Therefore, conditions (roll angle, Mach number) were not always ideally suited for FLEET data and were considered best effort. Finally, only facility condition data is valid during the tunnel warm up, not force and moment data or pressure port measurements due to the inability to keep systems calibrated with the transient temperature. Consequently, most results in this report derive from air runs.

During FLEET runs, the facility lights are dimmed to increase the contrast of the FLEET signal with respect to the background while still allowing nearly continual observation of the model by the test engineers. Three facility data acquisition system measurement points are acquired for each 32-point sweep, nominally near points 1, 17, and 32 in time, although the FLEET acquisition system is independent of the facility data acquisition system. For each measurement point, the laser shutter is commanded to open for 300 ms and ~ 222 images are acquired at 1 kHz, therefore each measurement point samples roughly 220 ms of the flow. However, as the images are divided between different measurement delays, each separate delay samples either 110 ms or only ~73 ms of the flow for the two-delay or three-delay strategy, respectively.

The temporal duration for each delay was selected to balance the camera memory and number of physical measurement positions (i.e., the memory is full after 64 points, or a 32-point sweep for +90° and -90°). Longer duration acquisitions would enable more images acquired per point but would limit the system to fewer physical measurement points. Unfortunately, the selected duration for each point is within or on the order of the observed period of model

oscillations. Within the plane of the detector (model x- and y-coordinate), oscillations of the model with respect to time were imaged at 1 kHz, revealing consistent ~10.8 Hz (93 ms period) and 67 Hz (15 ms period) oscillations in the y- and x-coordinates, respectively. While the magnitudes of the oscillations in the x-direction were small (~1 mm), those in the y-direction were much larger (0.32 inches or 8.1 mm on average peak-to-peak) and a significant fraction of the ~1 inch (25.4 mm) measurement length of the FLEET line. The FLEET line itself was found to also oscillate near 67 Hz with a magnitude of ~1 mm in the x-direction. Due to the low signal to noise ratio of the FLEET signal, all laser shots for each delay are averaged together regardless of the time within or magnitude of the model oscillations. This processing decision acts to degrade the spatial resolution in the y-direction of the measurement volume, encouraging viewing the full vertical bin (FVB) of each measurement point as opposed to the individual detector pixel values.

D. Fluorescence Fitting and Velocity Determination

Acquired FLEET signals were binned into their corresponding delays and averaged for each case to improve the signal-to-noise ratio. Seen in the top of Fig. 4, the intensity values in a local domain near the signal for each detector row are fit to a Gaussian function. Restrictions are placed on the full-width half-maximum and magnitude of the function to optimize the fits to the actual FLEET signal and not additional scattering on the model. The peak value of the Gaussian defines the physical position for each FLEET delay, where the spatially calibrated difference between delays coupled with the time difference defines the average velocity in the plane of the detector between the two points. Fig. 4 shows example fitting procedures for measurements in air. The useful velocimetry region along the y-axis was limited by the intensity of the zero-delay image along the beam waist. This intensity was fit with a Gaussian distribution, where intensities 30% or greater of the peak value were saved and the remainder discarded.

The limited length of the FLEET signal along the beam waist in air mode in comparison to the size of the wake and the model vibrations diminished the results to predominantly 1D measurements as seen in the far right of Fig. 4. However, the goal of the measurement campaign was to view the shear layer of the Orion model for a variety of conditions. Cryogenic nitrogen FLEET lines on average occur over twice the measurement domain in the y-axis, therefore enabling a more 2D view of the flow as opposed to the measurements in air. Fig. 5 shows a fitting example in cryogenic nitrogen at one measurement point in the shear layer. With the average FLEET lines at a singular point

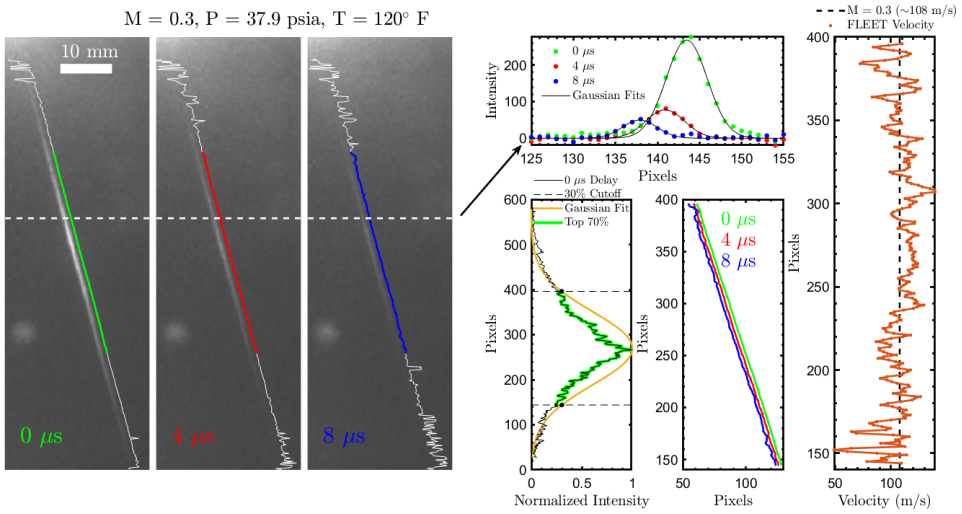

Fig. 4 Example fitting procedure in a near-freestream flow in air at M = 0.3 on the Abort heat shield (05052021, Run 7 point 8). The three average images for each delay are shown on the left with overlays of the fits in white purposefully offset from the raw signal. The bold color portion of the fit represents the top 70% intensity of the zero delayed acquisition as defined by the Gaussian fit to the zero delay image in the bottom center. Placing these fits on the same axis in the bottom of the figure shows a measurement line moving to the left (downstream) with increasing delay. An example fit for each delay is shown at the top of the figure for the highlighted row on the image. The resulting velocity determined from the 0 and 4 μs images is shown on the far right of the figure against the predicted freestream velocity for a Mach 0.3 flow at 120° F.

in the sweep pattern, the resulting velocity ranges from reverse flow high in the image to near freestream conditions lower in the image.

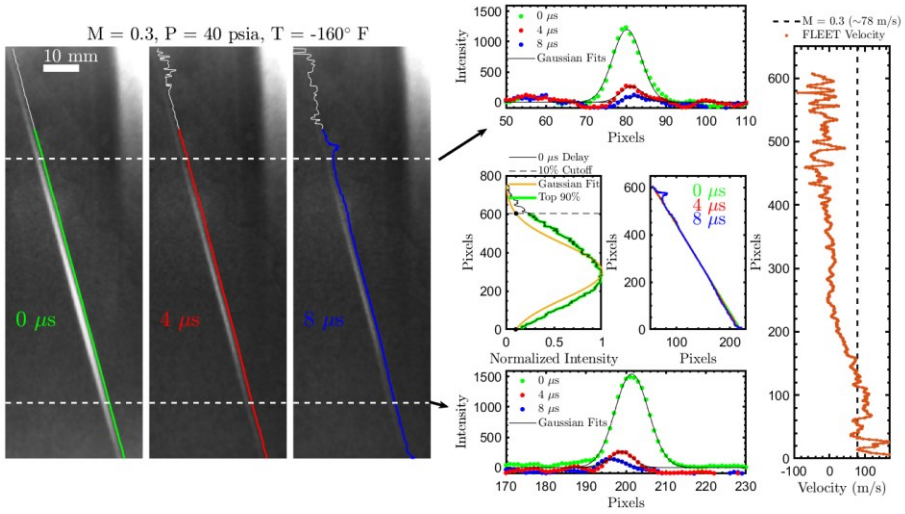

Fig. 5 Example fitting procedure for a measurement location in the shear layer of flow in cryogenic nitrogen at M = 0.3 (05262021, Run 8 point 4). The layout is similar to Fig. 4, where the three images on the left represent the average FLEET signal for each delay with the peak to the Gaussian fit overlaid in white for each row and in bold for the top 90% of the intensity of the zero-delay line. Fits near the top and bottom of the image show reverse flow (peaks moving to the right) and forward flow (peaks moving left) along the same line, resulting in the velocity profile on the far right.

III. Results

All results with reasonable signal to noise are shown here, beginning with the air data runs and the minimal relevant cryogenic nitrogen runs. The results are grouped by heat shield and presented in a common fashion of varying Mach number with column and Reynolds number with row when possible. Repeatability is discussed at the end of this section, whereas spatial and velocity uncertainties are included in the appendix.

A. Raw versus Smoothed Data

As averaged images for each delay, the result only offers a singular representation of the flow time integrated over a portion of the model and laser vibrations. This, in conjunction with the poor signal to noise ratio of the delayed data, leads to a noisy representation of the flow field. Therefore, for improved visualization, the raw measurement planes are smoothed using moving median filters three times: first in the vertical direction along the FLEET line, then in the horizontal direction from point-to-point, and then again in the vertical direction along the FLEET line. Fig. 6(a-b)

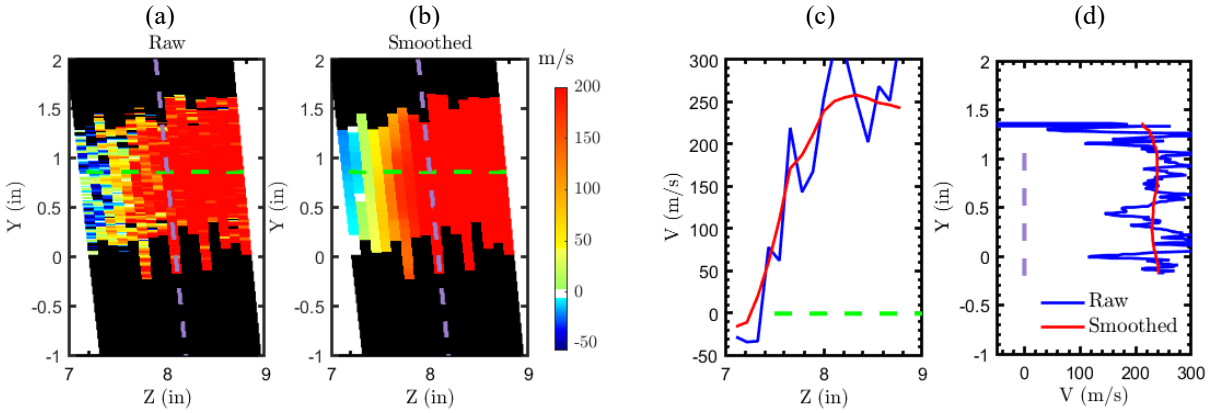

Fig. 6 Example smoothing process: (a) raw, 2D data and (b) smoothed 2D data with a horizontal (green) and vertical (purple) lines marked for realizations shown in (c) and (d), respectively.

shows an example of this smoothing process applied to one measurement plane of air data with specific lines highlighted in Fig. 6(c-d). Both the raw and smoothed data planes are shown in Fig. 7-8 for the IDAT filled datasets, but all other measurement planes in air are the smoothed results. These smoothed results are used for the full vertical bin analysis featured in the discussion.

B. Air Results: IDAT Heat Shield

Fig. 7 shows air results from the clean IDAT heat shield with model filler on the back shell when the model is rolled to +90° and mounted to the sting at 174°. The top two rows are the results from the raw fits to the 0 and 4 μs data, whereas the bottom two rows are the same data smoothed by the method from Fig. 6. As defined earlier, for each physical location the extent of the measurement in the y-direction is defined by the top 70% of the intensity from the zero-delay image, therefore the vertical position for each plane deviates slightly from point to point, but overall the measurement range in the y-axis is ~1 in or greater. Due to the fixed position of the sweep mirror and the inability to remotely change the beam focus, the absolute position on the y-axis is biased with position within a measurement plane and from the upstream to downstream planes. In general, points further from the model are physically higher in

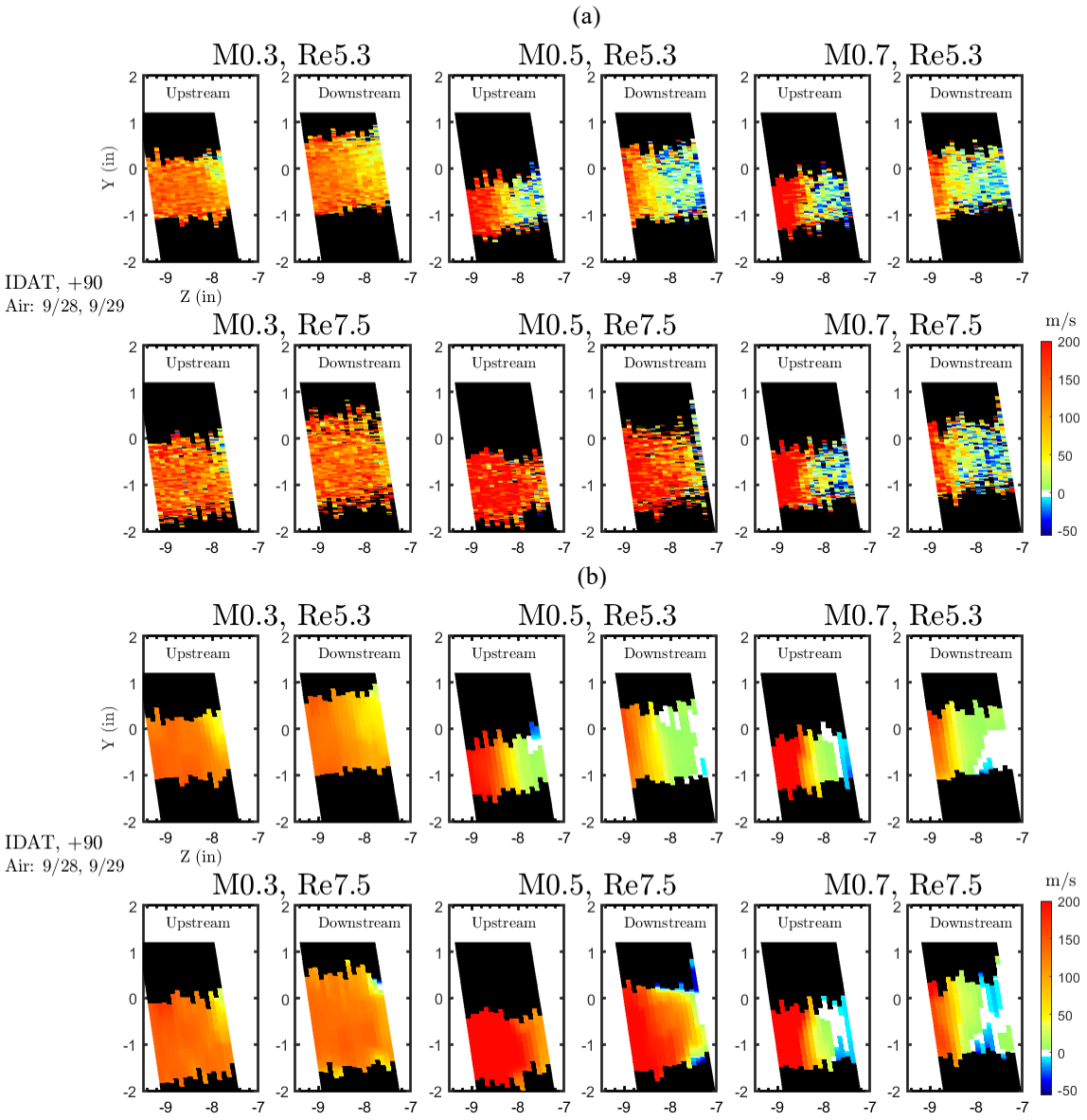

Fig. 7 Comparison of IDAT filled back shell (a) air data raw results to (b) smoothed results for +90° roll.

the tunnel (more negative for the +90° roll model frame y-axis and more positive for -90° roll) and the downstream plane is always physically lower in the tunnel (more positive for the +90° roll model frame y-axis). These trends are consistent throughout the results.

The measurement objective was always to find and measure the shear layer for each condition. The color map for the contour plots remains consistent throughout the manuscript and depicts blue as reverse flow, white as velocity near 0 m/s, and green/yellow/orange/red as the progression towards higher positive magnitude velocity. Therefore, any transition from blue to orange/red represents flow from the wake to near freestream conditions. For the +90° roll cases in Fig. 7, the M = 0.5 and 0.7 cases all exhibit signs of the measurement planes translating through the wake of the model, whereas the M = 0.3 measurements all show positive flow with a much weaker velocity deficit featured closer to the model (right side of each plot) suggesting the measurement planes were too far away from the model for those cases. In general, the wake moves out (more negative in the model z-coordinate) with increasing Mach number and with downstream position, but changes with Reynolds number for the M = 0.3 and M = 0.7 cases appear insignificant with this level of data quality. However, for M = 0.5 the wake appears to shrink with increasing Reynolds number from 5.3 to 7.5 million in both the upstream and downstream planes.

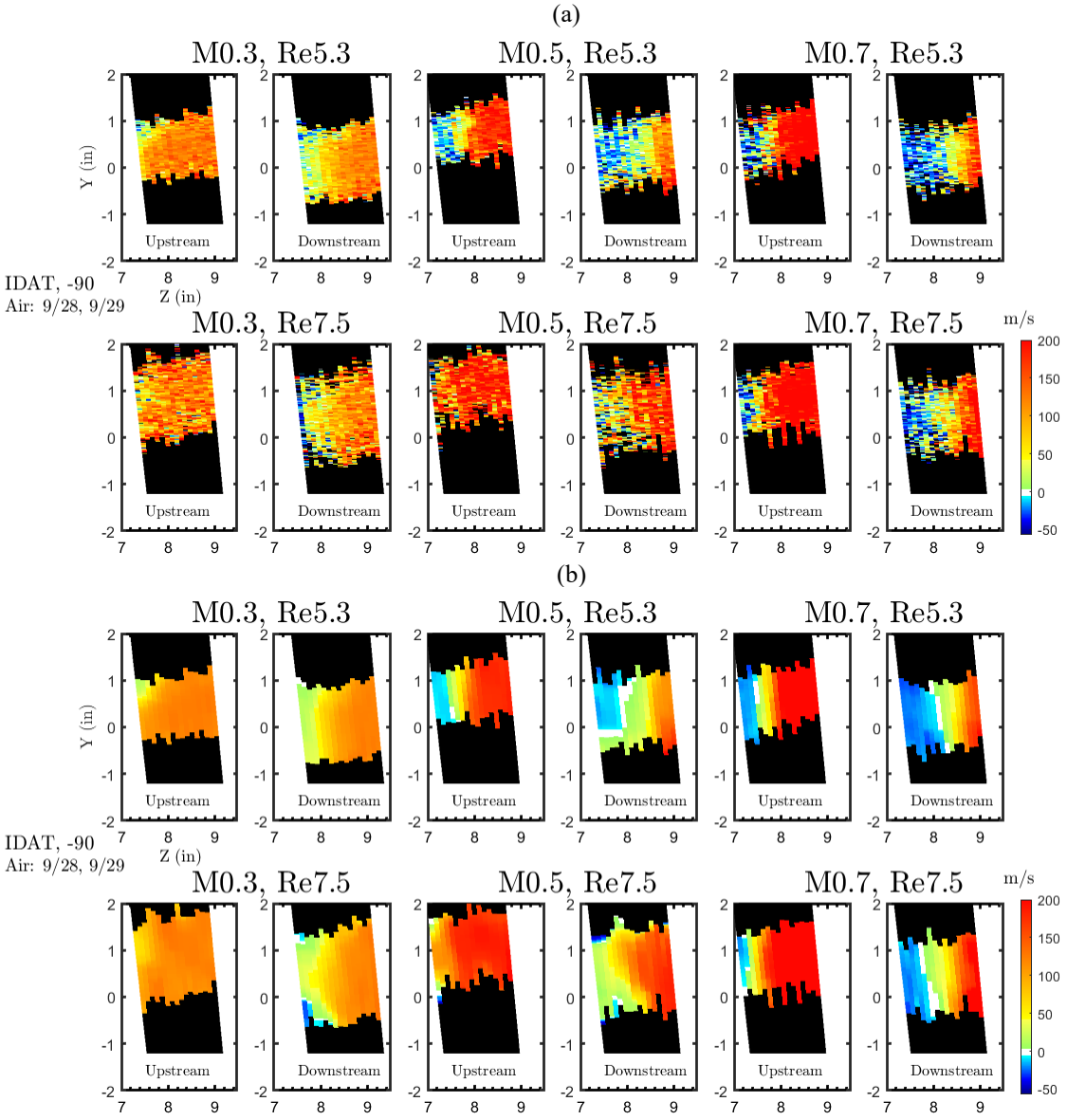

Fig. 8 Comparison of IDAT filled back shell (a) air data raw results to (b) smoothed results for -90° roll.

Similar to the +90° roll case of Fig. 7, the -90° roll measurements of the IDAT heat shield are shown in Fig. 8(a) and (b) for the raw results and smoothed results, respectively. The trends on this side of the model are near identical to those from the +90° roll case. A velocity deficit is barely seen in the M = 0.3 data, but clearly present for M = 0.5 and M = 0.7. The wake size increases with increasing Mach number and downstream position, with insignificant Reynolds number effects for the M = 0.3 and M = 0.7 cases. However, once again the M = 0.5 case shows a decrease in the size of the wake with increasing Reynolds number.

From here on, beginning with the IDAT heat shield without model filler on the back shell in Fig. 9, the presented results are only the smoothed contours. Also note that unlike the IDAT heat shield data with a filled back shell, a number of the remaining heat shield cases have incomplete datasets due to time limitations during data acquisition resulting in many of the FLEET data points being skipped. Therefore, only partial comparisons are available.

As far as the FLEET instrument is concerned, the observed difference between model filler and no model filler is negligible. The heat shield geometry remains the same, and the majority of the model filler locations on the back shell were downstream from the FLEET measurement volume or rotated away from the measurement region. Therefore, repeating the same conditions would be expected to be equivalent to repeat runs. Therefore, for the IDAT heat shield measurements without model filler presented in Fig. 9, Mach numbers of 0.4 and 0.6 were selected as opposed to the standard 0.3 and 0.5 to expand the scope of the testing since sufficient repeat runs were already included in the text matrix. The same Reynolds numbers of 5.3 and 7.5 million were used, except for the M = 0.4 case, where the pressure was incorrectly set resulting in a Reynolds number of 4.7 million.

Once again, the location of the shear layer for all cases moves outward with both downstream position and increasing Mach number. For the M = 0.4 cases, the wake decreases with increasing Reynolds number for both +90° roll and -90° roll. Although the lower case is at a Reynolds number of 4.7 as opposed to 5.3 million, this trend is consistent with the filled IDAT heat shield M = 0.5 case. Trends with Reynolds number at M = 0.6 are less obvious, as the profiles appear similar for the +90° roll yet differ for -90° roll, showing once again the increase in the wake size with decreasing Reynolds number. While no repeat runs were available to confirm these points, these runs do show the continuation of this Reynolds number effect on the wake stretched from M = 0.4 to M = 0.6 for at least the -90° roll case but ends at M = 0.3 and M = 0.7 respectively. This may suggest M = 0.3 remains a more laminar flow consistently over the heat shield while the M = 0.7 cases are turbulent with the M = 0.4-0.6 cases being in between leading to a change in wake profile with respect to Reynolds number.

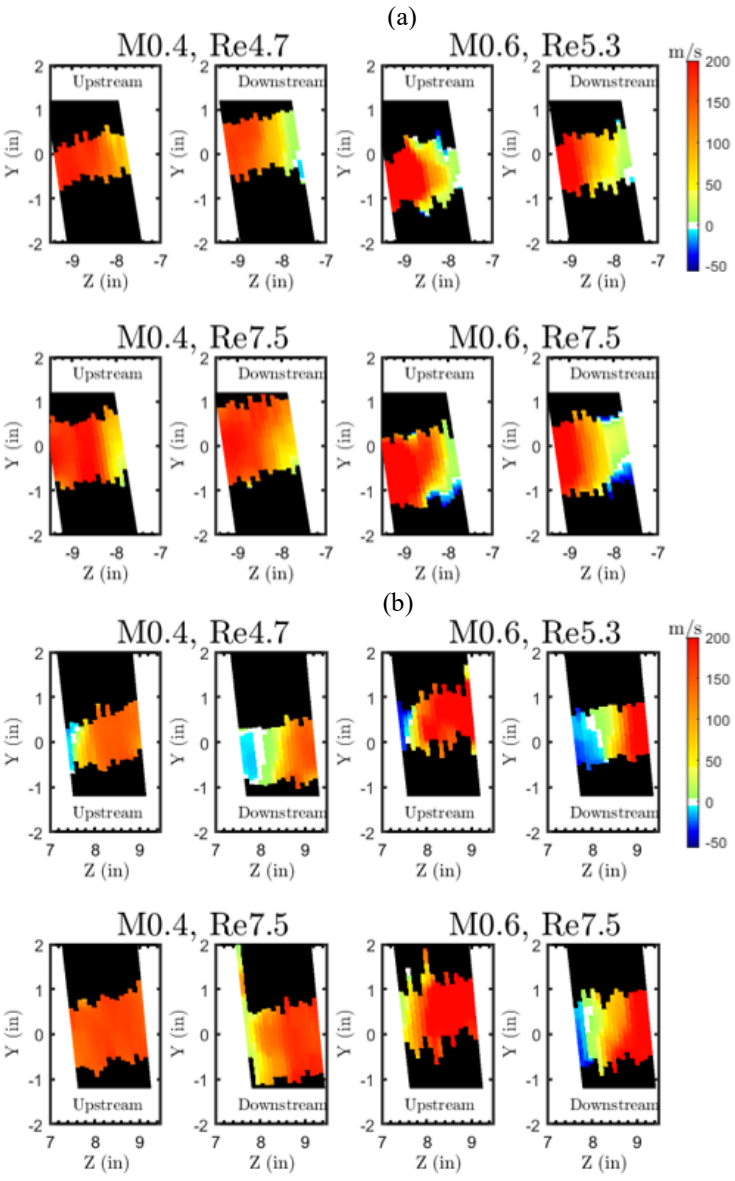

Fig. 9 Comparison of smoothed IDAT heat shield data without model filler in the back shell for (a) +90° roll and (b) -90° roll. (Data from 10/20/21)

Fig. 10 shows limited results at a singular Reynolds number of 7.5 million from the IDAT heat shield with the addition of fine grit and without model filler on the back shell. For comparison purposes, Fig. 10(a) and Fig. 10(b) relate directly to the corresponding clean heat shield results of Fig. 7 and Fig. 8, respectively. With grit added to the heat shield, the flow is disturbed/tripped, encouraging a turbulent boundary layer around the vehicle. With this added roughness, the clean heat shield trend with an increase in wake size with increasing Mach number is diminished, as the position of the wake for both the M = 0.3 and M = 0.5 cases are near identical to each other. However, the wake continues to increase with downstream position for each case. Finally, in comparison to the clean heat shield cases,

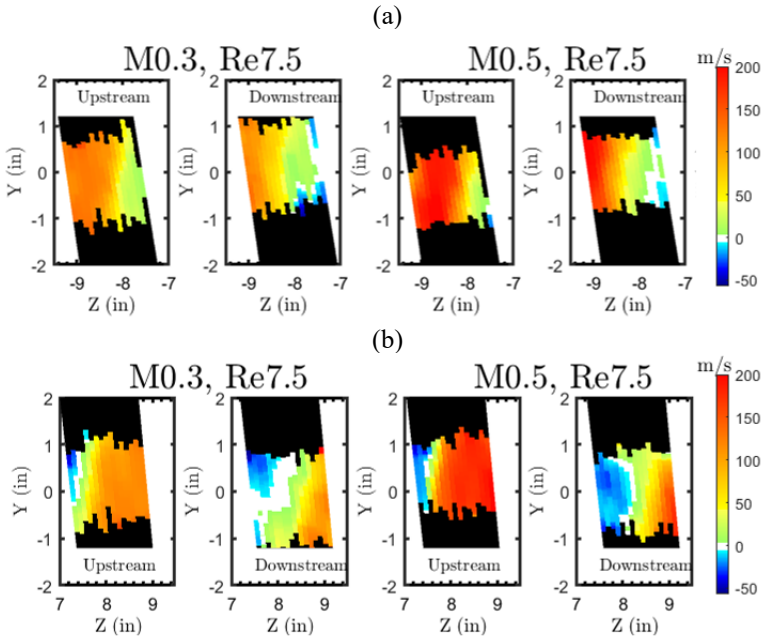

Fig. 10 Comparison of smoothed IDAT heat shield with fine grit without back shell model filler data for (a) +90° roll and (b) -90° roll. (Data from 11/15/21)

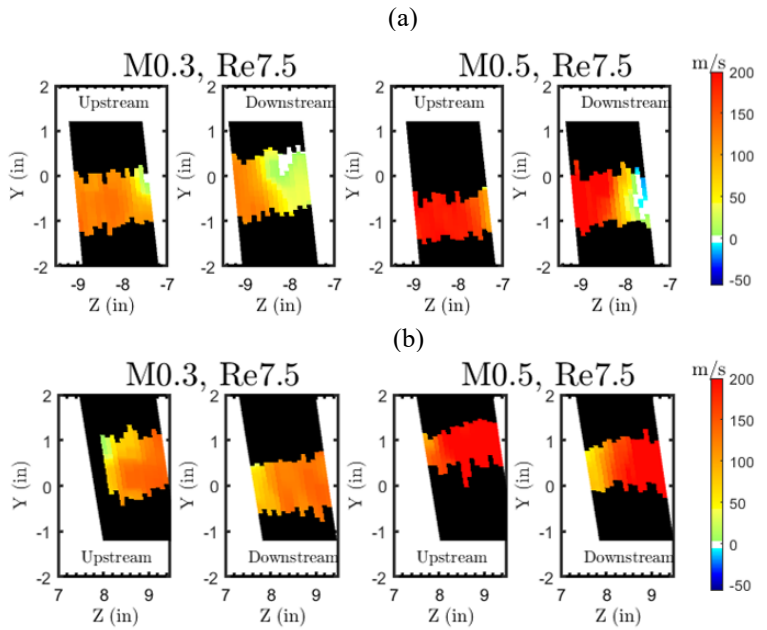

Fig. 11 Comparison of smoothed 186° IDAT heat shield without back shell filler data for (a) +90° roll and (b) -90° roll. (Data from 10/12/21)

the wake is larger for all four runs (M = 0.3 and 0.5 at Re = 7.5 million) with the increase in heat shield surface roughness.

The remaining IDAT heat shield runs (Fig. 11 and Fig. 12) are all with the model mounted to the sting at an angle of 186° as opposed to 174°. Regarding the heatshield and location of the FLEET measurement volume, this mounting configuration should be perfectly symmetric (e.g. +90° roll for the 174° mounting angle should be the same as the -90° roll case for the 186° mounting angle). Therefore, Fig. 7b should be mirrored of Fig. 11a and Fig. 8b should be mirrored of Fig. 11a. This is roughly true, as the side of the model angled towards the measurement volume results in a larger wake for each case (-90° roll for 174° mounting angle and +90° roll for 186° mounting angle).

Fig. 12 shows a complete set of results from the IDAT heat shield mounted at 186° with grit added to the surface and offers a more direct comparison to the free transition (clean heat shield) data of Fig. 11. As seen with the earlier fine grit data, the fixed transition of the heat shield boundary layer results in a larger wake than the free transition and the position appears independent of the flow Mach number. These runs also offer a Reynolds number comparison for

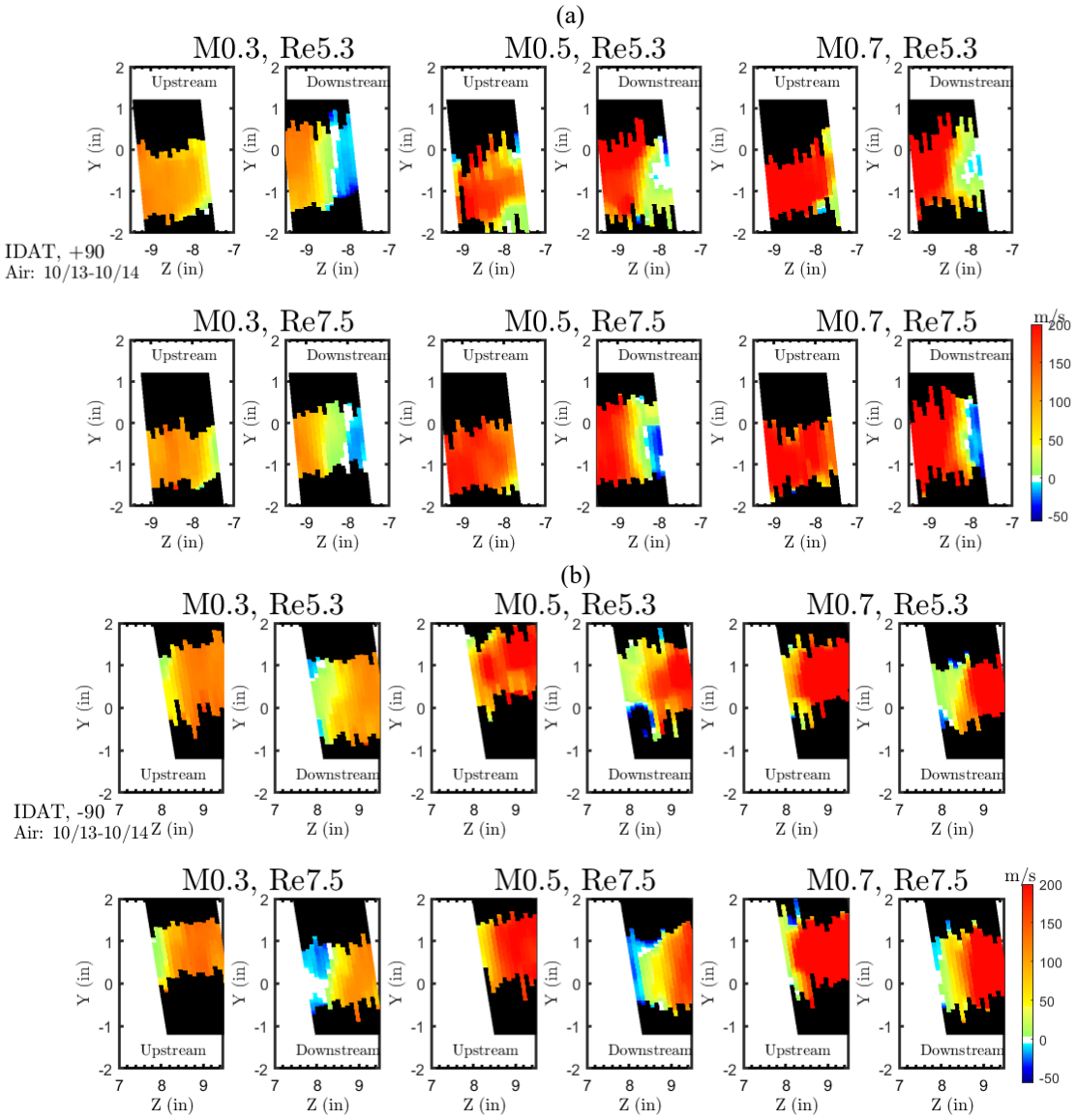

Fig. 12 Comparison of fixed transition 186° IDAT with grit data for (a) +90° roll and (b) -90° roll. (Data from 10/13 to 10/14).

fixed transition cases, although similar to the change in the Mach number, a change in Reynolds number from 5.3 to 7.5 million appears negligible in the position of the wake.

C. Full Vertical Bin and Measurement Repeatability

In air mode, the measurement length along the beam waist (predominantly in the model frame y-axis) is ~1 in and comparable to the magnitude of the model vibrations which degrades the natural detector resolution in the model y-axis. Luckily, the streamwise velocity gradients in the y-direction are expected to be less than those in the z-direction near the centerline of the model. The results are already time-averaged over the course of the model vibrations and oscillations, therefore a full spatial average in the vertical axis voids the uncertainty in y-coordinate spatial resolution by sacrificing all resolution down to a single measurement line representing an average over the full y-axis. Each measurement is predominantly within 1 inch of the tunnel centerline (-1 in to 1 in depending on the roll angle), therefore this spatial average is assumed to be a good approximation of the wake profile at y = 0. This method is titled full vertical binning (FVB) throughout the remainder of the document.

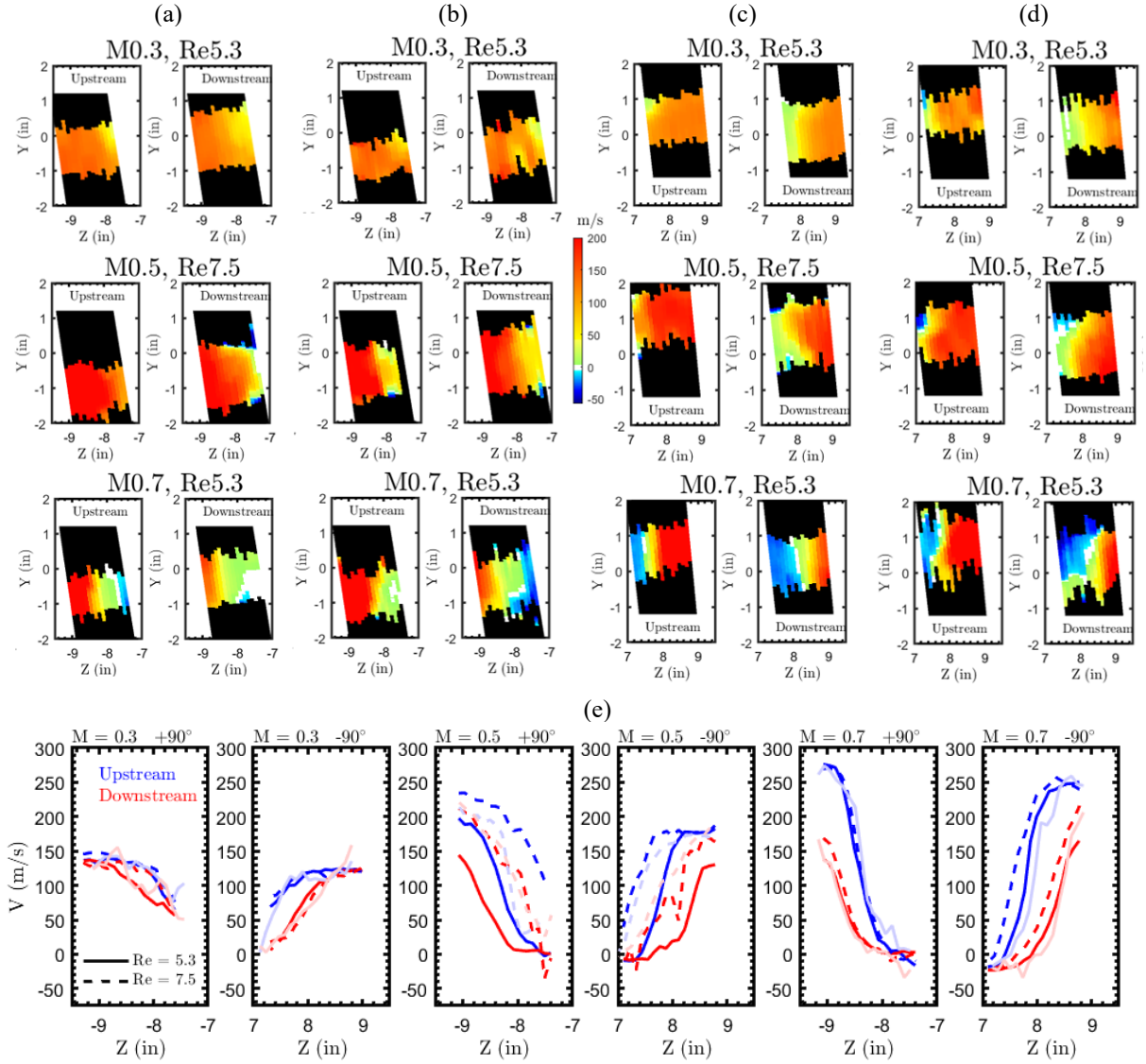

Fig. 13 (a,c) Original air runs for the IDAT filled heat shield for a +90° and -90° roll, respectively with the (b,d) corresponding repeats, summarized in the full vertical bin results in (e) with faded curves indicating the repeated runs. Compare across rows of (a-b) and (c-d).

This FVB method enables a simplified form of direct comparison between repeat runs, which themselves are critical due to the uncertainty in the temporal behavior of the acquired average measurements. Fig. 13 shows original IDAT runs (a, c) against repeat runs (b, d) and summarized in FVB plots (e). Repeat runs were not performed for all cases, therefore only strategic Mach and Reynolds numbers were selected for repeats to provide confidence the acquired measurements are an accurate presentation of the actual flowfield. Visual comparison of the contour plots (compare rows in (a) and (b) for +90° roll and (c) and (d) for -90° roll) show reasonable agreement, but the FVB plots in Fig. 13(e) offer a more quantitative comparison. In these FVB plots, the color defines the upstream (blue) and downstream (red) position with solid curves showing cases with a Reynolds number of 5.3 million and dashed curves showing a Reynolds number of 7.5 million. Repeat runs are faded colors. For Fig. 13(e), all the results from the original runs are included against the limited repeats to show how the repeat runs compare against the opposite Reynolds number original run case. This comparison is critical to confirm measurement cases with observed Reynolds number dependence, such as the M = 0.5 case for the IDAT heat shield (center two subplots in Fig. 13(e)).

Outside of the upstream Re = 7.5 million, M = 0.5 measurement plane, all repeats agree reasonably well with the original runs. For M = 0.3 at +90° roll, the downstream plane at Re = 5.3 million deviates from the others with a lower velocity profile and is replicated with the repeat run whereas the upstream repeat matches the original profiles. For the -90° roll, there are two well defined groups of profiles for the upstream and downstream planes with the repeats confirming the behavior. The M = 0.5 repeats are again of significant interest, as this case revealed a significant Reynolds number effect on the wake position. These repeats are for Re = 7.5 million (dashed lines) and the solid lines from Re = 5.3 million are included for comparison, showing a larger wake with smaller Reynolds number. For the repeat runs at +90°, both the upstream and downstream planes are near identical to each other and match the original downstream run whereas the upstream run has a higher velocity overall. Both Re = 5.3 million runs are lower in velocity (i.e., larger wake) than all original and repeat 7.5 million runs. For -90° roll, the repeats follow the trends of the originals, where again the 5.3 million runs show a larger wake. Finally, the M = 0.7 cases also offer clear groupings of upstream and downstream velocity profiles, with minimal difference with Reynolds number and good agreement with the repeat runs. In summary, these repeats do offer confidence in the ability to measure a true representation of the flowfield even with the limited temporal duration of each measurement point.

Fig. 14 shows repeat runs for the fixed transition IDAT heat shield mounted at a 186° angle on the sting. As mentioned previously, the fixed transition cases seem to promote wake profiles that are independent of Mach and Reynolds numbers for the range of these measurements. While the profiles are not as clean as the free transition IDAT heat shield profiles, the repeat runs at Re = 7.5 million once again agree well with the original runs.

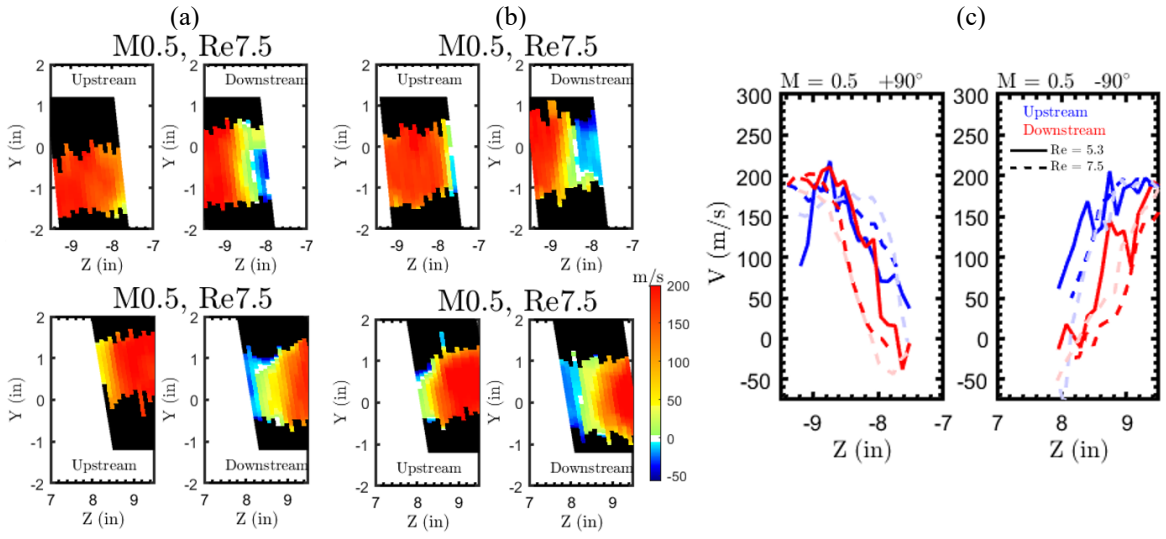

Fig. 14 (a) Original runs from 10/13/2021 for +90° (top row) and -90° roll (bottom row) and (b) repeat measurement planes from 10/14/2021 with coinciding (c) full vertical bin original (bold) and repeat (faded) runs for the 186° mounted IDAT heat shield with grit.

IV. Discussion

This section acts to analyze the previously presented results for measured differences in the heat shields, Mach number effects, Reynolds number effects, and the effect of surface roughness. Due to the transient and scarce results in cryogenic nitrogen, this analysis is limited to the results in air. To clarify the notation in this section, an increase in the wake profile represents the movement of the shear layer away from the model, while a decrease in the wake profile depicts the shear layer moving closer to the model.

D. Trends with Mach and Reynolds number

Basic trends with Mach number at constant Reynolds number are highlighted in Fig. 15 for the IDAT heat shield. The IDAT runs also include cases at M = 0.4 and M = 0.6 without model filler on the back shell which should have a negligible effect on the measurement volume due to the downstream location if model filler. Note that the M = 0.4 lower Reynolds number case is at 4.7 million as opposed to all others at 5.3 million. The average x-positions for all measurements profiles are also included in each plot to either demonstrate a similar measurement volume or explain differences in the average profile.

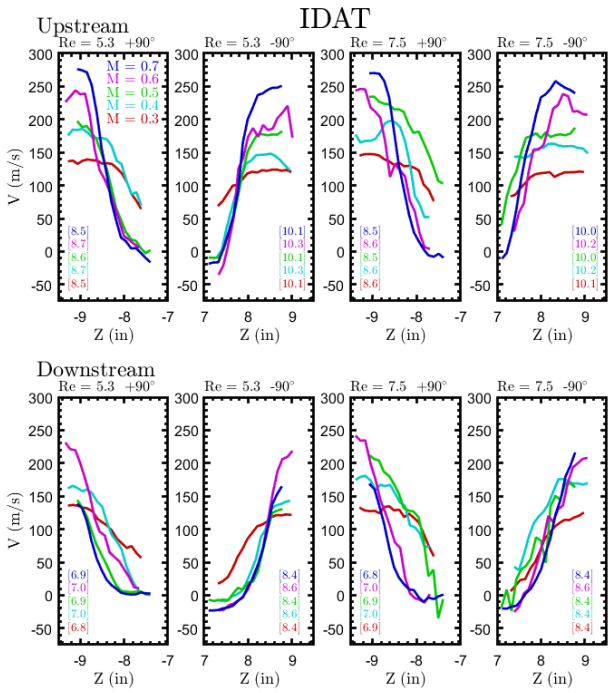

Fig. 15 Mach number dependence of the IDAT heat shield with free transition for the upstream (top row) and downstream (bottom row) measurement planes. Note that the Reynolds number at Mach = 0.4 is 4.7 million, not 5.3 million.

The downstream IDAT data in Fig. 15(a) features grouped velocity profiles that more regularly collapse onto a similar curve for all -90° cases (second and fourth column), whereas the +90° orientation results in a larger spread in velocity profile dependent on the Mach number (first and third columns). A likely source of this difference is in the geometry of the model with respect to the flow for each of these cases. For a smooth, free transition heat shield, the more gradual flow change offered by the +90° roll configuration (red profile from Fig. 3(b)) is likely affected more by small changes in the heat shield boundary layer which propagate downstream and alter the shear layer. The spread in observed profiles features a general Mach number dependence, with increasing wake size with increasing Mach number. The Re = 5.3 million, +90° case is a prime example of this, with the M = 0.3, 0.4, and 0.5 curves all coalescing inward to a common profile separate from a common M = 0.6 and 0.7 curve. The -90° configuration protrudes further into the flow, offering a larger turning angle for the incoming flow with a coinciding larger region of flow recirculation. This more abrupt configuration is likely less sensitive to small variations in the heat shield boundary layer, leading to a more consistent location of the shear layer as a function of Mach number. For Re = 5.3 million, only the M = 0.3 profile differs from the others at -90°, whereas the 7.5 million profiles all appear to coalesce to common profiles, albeit with less precision than the 5.3 million cases. All cases show an increasing wake with downstream position.

Reynolds number trends at constant Mach number are viewed exclusively on the IDAT heat shield in Fig. 16 for the (a) +90° roll and (b) -90° roll configurations. Note that while all comparisons are between 5.3 million (solid) and 7.5 million (dashed) Reynolds numbers, the lower M = 0.4 Reynolds number is 4.7 million (solid) due to the total

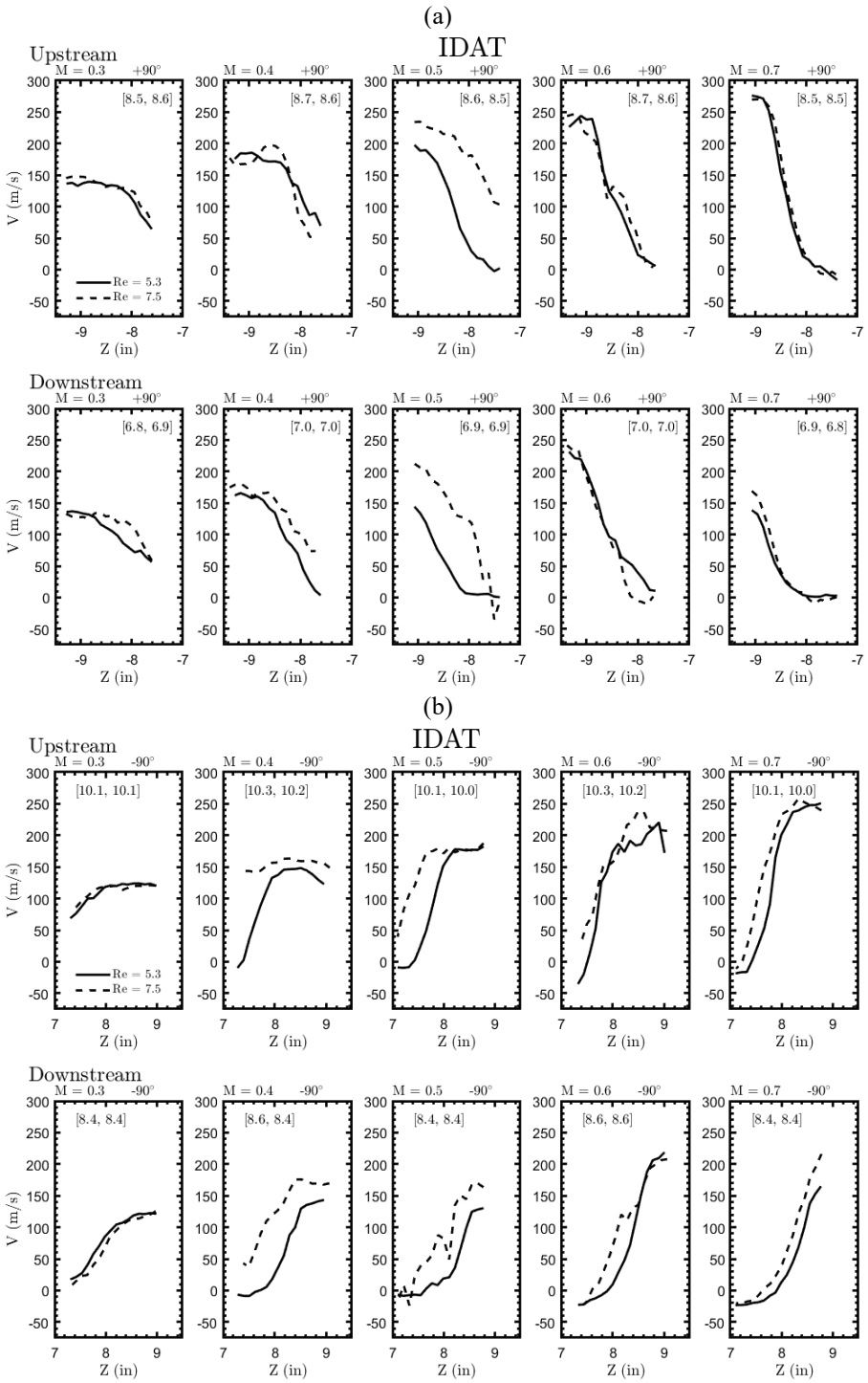

Fig. 16 Reynolds number dependence for the IDAT heat shield at (a) +90° roll and (b) -90° roll. For all M = 0.4 cases, the lower Reynolds number is 4.7 million, not 5.3 million. The average x-coordinate for each profile is included in each sub figure for [Re = 5.3 million, 7.5 million] in inches.

pressure in the tunnel set to the static pressure value. While this does limit the direct comparison, it still offers a high-low Reynolds number comparison for each Mach number.

For all M = 0.3 measurement planes (first column), there is no obvious Reynolds number dependence, as the 5.3 and 7.5 million profiles overlap for both upstream and downstream positions. The same is true of the M = 0.6 (fourth column) and the M = 0.7 (fifth or last column) measurements within spatial uncertainty. However, for some of the M = 0.4 and all of the 0.5 cases, there is a distinct change in profile with Reynolds number. For M = 0.4, the profiles at +90° appear consistent for Re = 4.7 and 7.5 million, with a slight deviation in the downstream plane depicting a larger wake with the lower Reynolds number. For the -90° configuration, this trend is more pronounced, with the 4.7 million Reynolds number case depicting a larger wake in both upstream and downstream planes. This trend is amplified for all M = 0.5 measurement planes, where the decrease in Reynolds number leads to a larger wake profile. While unable to precisely compare the 5.3 million Reynolds number case of M = 0.5 to the Re = 4.7 million case of M = 0.4, the data do show a Reynolds number dependence of the wake at intermediate subsonic Mach numbers.

This observation of common profiles with Reynolds numbers at low Mach and high subsonic Mach numbers with variance in between suggests these measurements are integrating over conditions encompassing the laminar to turbulent transition and separation of the flow passing over the heat shield and into the shear layer. For low Mach number, the flow could be laminar regardless of Reynolds number (within the range investigated here). For high subsonic Mach numbers, the flow appears turbulent with possible separation regardless of Reynolds number. However, for intermediate Mach numbers, the flow appears to transition from laminar to turbulent based on the Reynolds number, leading to a change in the shape of the wake off the model shoulder.

E. Effect of Surface Roughness

The addition of grit to the heat shield surface created fixed laminar to turbulent transition conditions on the heat shield boundary layer which propagate into the wake and thus the FLEET measurement volume. Fig. 17 depicts the effect of grit addition to the IDAT heat shield as a function of Mach and Reynolds number. Three different heat shield configurations are shown, with the standard clean free transition IDAT shield in blue, the addition of fine grit to the IDAT heat shield in light blue, and finally the addition of normal grit to the surface in red. Note the case with normal

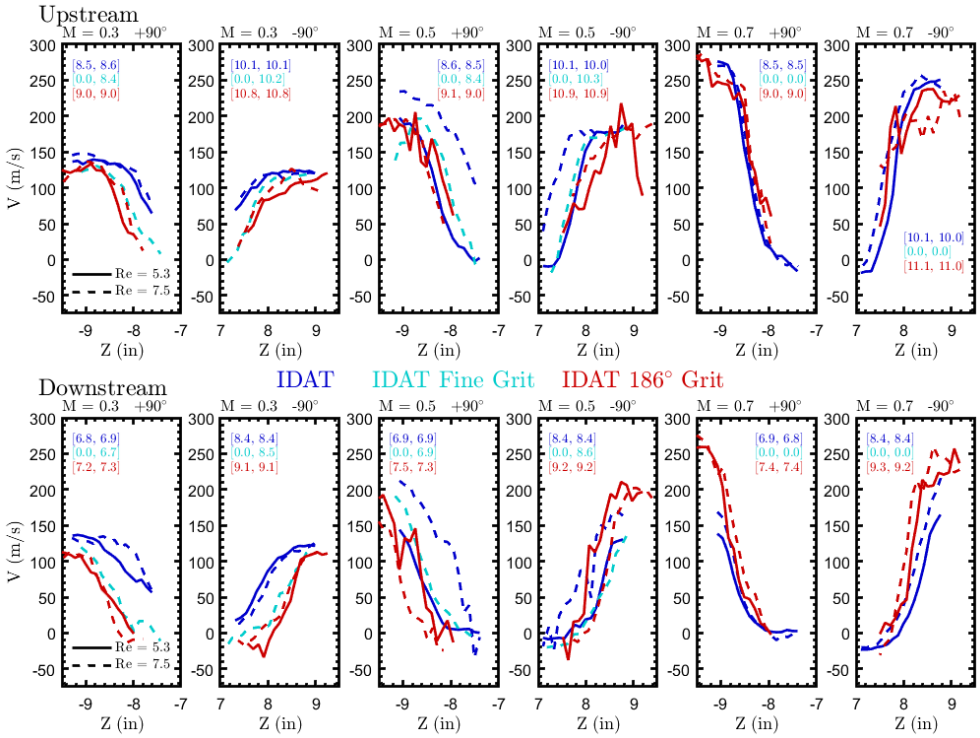

Fig. 17 Dependence of surface roughness on the wake profile position for the IDAT heat shield with free transition (blue), the addition of fine grit (light blue) and the addition of grit (red). Average x-locations for each profile are included in inches with the following format: [Re = 5.3 million, Re = 7.5 million]. X = 0 denotes no data available for those conditions.

grit was mounted to the sting at an angle of 186° (as opposed to all unlabeled cases at 174°), and the results were deemed symmetric and therefore flipped to match those of the standard 174° mounting angle (e.g. the -90° roll case for a 186° mounting angle is shown as the +90° roll case and vice versa). An unintended artifact of this difference in mounting angle is the increase in average x-location for each 186° case of 0.4 to 1.0 inches compared to the 174° cases. This upstream x-position of the fixed transition cases would suggest a smaller wake profile if the heat shields were constant as the wake increases with downstream position, but as seen in the data this is not the case. For all M = 0.3 and 0.5 measurements, the addition of grit acts to move the shear layer away from the model. For M = 0.3 specifically, all four measurement planes show distinct groupings of the free transition profiles (blue) independent of a separate fixed-transition grouping (light blue and red). At M = 0.5, the fixed transition cases match the profiles of the 5.3 million Reynolds number cases from the free transition heat shield, all of which exhibit larger wake profiles than the 7.5 million cases. Finally, at M = 0.7 both the free and fixed transition cases coalesce onto a common profile for both upstream and downstream measurement planes, with the fixed profiles slightly inward from the free profiles. However, given that the fixed transition cases are further upstream than the coinciding free transition results, fixed transition profiles at the same x-locations as the free transition measurements may show larger wake profiles and act to improve the overlap between the two cases.

In conclusion, the addition of grit to the heat shield acts to increase the wake size of normally smooth heat shields at lower Mach numbers, match the 5.3 million Reynolds number free transition profiles at M = 0.5 for Re = 7.5 and 5.3 million, and appears to have no effect on the measurement wake profiles of the M = 0.7 flow case. This line of results suggests the addition of surface grit negates the Mach number dependence of the measurement wake profile, given that, as seen before with the free transition Mach number dependence of Fig. 15, the lower Mach number cases experience smaller wake profiles than their higher Mach number counterparts. Therefore, by increasing the wake size of lower Mach cases only, the addition of surface roughness would coalesce all the Mach number profiles onto a common wake profile curve. Fig. 18 shows this Mach number independence of the IDAT heat shield with grit mounted at 186° on the sting (i.e. the red curves from Fig. 17). As compared to the free transition data, now all wake profiles appear to follow similar trends, albeit with low precision.

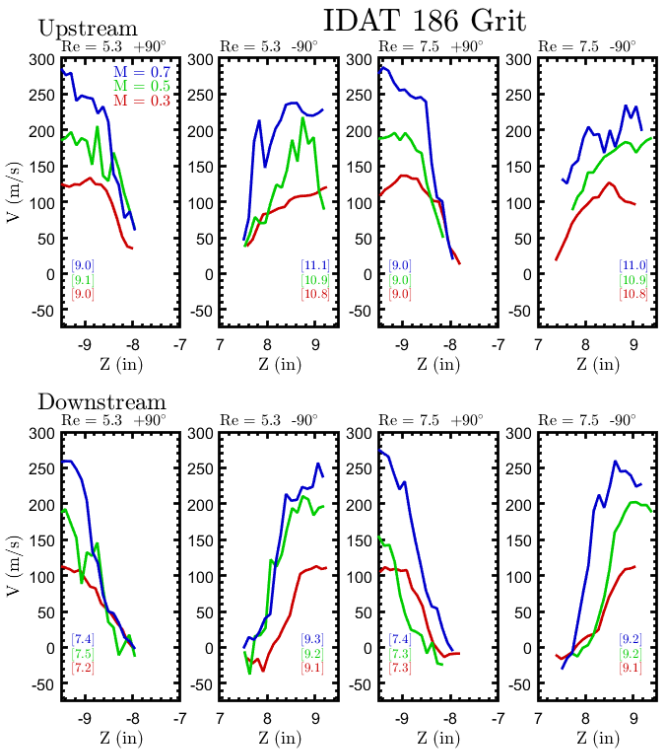

Fig. 18 Mach number dependence for constant Reynolds number for the IDAT heat shield with grit (fixed transition). Average x-locations for each profile are included in inches in square brackets.

V. Conclusion

The molecular tagging technique, FLEET, was applied to measure the subsonic wake profiles of the Abort, IDAT, and Fenced heat shields of the Orion model in both free transition and fixed transition cases at Reynolds numbers of 5.3 and 7.5 million in air mode at the National Transonic Facility with only the IDAT results presented in this work. At higher Reynolds numbers in cryogenic nitrogen, a limited number of useful runs were measured under transient conditions during the facility warm up to avoid the otherwise stochastic nature of the location of the FLEET signal throughout the detector field of view. While pure nitrogen acted to increase the measurement length of the system, it remained unreliable throughout the test, leading to the vast majority of deliverable results restricted to air mode. For most runs, an automated discrete 32-point 2-plane sweep pattern was employed on the far side of the model to capture an upstream and downstream view of the wake profile with the model rolled to +90° and -90°.

The geometry of the laser delivery to the test section coupled with the reverse flow and turbulent wake over the long test duration made it challenging to acquire reasonable signal-to-noise level FLEET signals that adequately captured the true features of the flow. Therefore, all common delay images for each spatial location were averaged to

improve the quality of the spatial fits, although this included temporal averages over incomplete periods of the model oscillations. The slow speed of the motorized sweep mirror and camera memory limited the instrument to ~3 minutes per 32-point sweep and a total of 64 measurement points, respectively, before the operator was required to wait until all data was saved. In the future, diminishing the angle of the laser delivery through the port window will improve the signal strength, acquiring a faster motorized mirror will increase the speed of data acquisition, and acquiring a camera system with more memory and faster download will enable more continuous data acquisition.

The 2D velocity planes measured for each heat shield configuration stressed the importance of accurate absolute spatial positions for each measurement plane. The model x- and y-coordinates are based on the detector field of view, whereas the z-coordinate predominately out of the detector plane was determined by imaging the beam spot on the tunnel floor and relating the position back to the center of the test section next to the model. For the M = 0.5 and 0.7 cases, the shear layer was routinely measured for all upstream and downstream cases. However, for the M = 0.3 case, the measurement volume was on the outer extent of the shear layer, with only the inner most points catching a portion of the velocity deficit. By degrading the measurement resolution in the model y-axis to counteract the oscillating model during the temporal average of the measurement, FVB comparisons between heat shields and over Mach and Reynolds numbers are presented. For free transition heat shield configurations, the measured wake profiles increased with increasing Mach number for constant Reynolds number. For M = 0.3 and 0.7 cases, the wake profile appeared insensitive to changes in Reynolds number, but at M = 0.5 the higher the Reynolds number the smaller the observed wake profile. The addition of surface roughness negated the Mach number dependence by expanding the wake profiles of smaller Mach number flows with negligible changes to higher Mach number runs.

Acknowledgments

The authors appreciate the assistance and expertise of the entire NTF staff. This test was not possible without significant efforts from almost all members of the staff. Additional thanks to Neil Rodrigues (NASA Post-doctoral program) for covering some tunnel runs, and Christopher Dupuis (Universities Space Research Association) for some of the model frequency work. The other researchers were supported by the Aerosciences Evaluation and Test Capabilities (AETC) Portfolio, Test Technology Focus Area under the leadership of James Bell initially, and later David Stark.

References

[1] NASA. “Exploration Systems Architecture Study.” 2005, p. 758.

[2] Murphy, K. J., Borg, S. E., Watkins, A. N., Cole, D. R., and Schwartz, R. J. “Testing of the Crew Exploration Vehicle in NASA Langley’s Unitary Plan Wind Tunnel.” *Collection of Technical Papers - 45th AIAA Aerospace Sciences Meeting*, Vol. 17, No. January, 2007, pp. 12155–12179. https://doi.org/10.2514/6.2007-1005.

[3] William C. Moseley, Jr., and J. C. M. “APOLLO WIND TUNNEL- TESTING PROGRAM - HISTORICAL DEVELOPMENT OF GENERAL CONFIGURATIONS.” *NASA TN D-3748*, 1966.

[4] Bell, J. H. “Transonic/Supersonic Wind Tunnel Testing of the NASA Orion Command Module.” *Collection of Technical Papers - 45th AIAA Aerospace Sciences Meeting*, Vol. 17, No. January, 2007, pp. 12180–12214. https://doi.org/10.2514/6.2007-1006.

[5] Ross, J. C., and Brauckmann, G. J. “Aerodynamic and Aeroacoustic Wind Tunnel Testing of the Orion Spacecraft.” *29th AIAA Applied Aerodynamics Conference 2011*, No. June, 2011, pp. 1–19. https://doi.org/10.2514/6.2011-3160.

[6] Murphy, K. J., Bibb, K. L., Brauckmann, G. J., Rhode, M. N., Owens, B., Chan, D. T., Walker, E. L., Bell, J. H., and Wilson, T. M. “Orion Crew Module Aerodynamic Testing.” *29th AIAA Applied Aerodynamics Conference 2011*, No. June, 2011, pp. 1–23. https://doi.org/10.2514/6.2011-3502.

[7] Bibb, K. L., Walker, E. L., Brauckmann, G. J., and Robinson, P. E. “Development of the Orion Crew Module Static Aerodynamic Database, Part II: Supersonic/Subsonic.” *29th AIAA Applied Aerodynamics Conference 2011*, No. June, 2011, pp. 1–34. https://doi.org/10.2514/6.2011-3507.

[8] Bibb, K. L., Walker, E. L., Brauckmann, G. J., and Robinson, P. E. “Development of the Orion Crew Module Static Aerodynamic Database, Part I: Hypersonic.” *29th AIAA Applied Aerodynamics Conference 2011*, No. June, 2011, pp. 1–23. https://doi.org/10.2514/6.2011-3506.

[9] Oravetz, C. T., and Yechout, T. R. "Experimental Investigation of the Wake Characteristics of the NASA Orion Capsule." *46th AIAA Aerospace Sciences Meeting and Exhibit*, No. January, 2008, pp. 1–11. https://doi.org/10.2514/6.2008-831.

[10] Brown, J. D., Bogdanoff, D. W., Yates, L. A., and Chapman, G. T. "Transonic Aerodynamics of a Lifting Orion Crew Capsule from Ballistic Range Data." *Journal of Spacecraft and Rockets*, Vol. 47, No. 1, 2010, pp. 36–47. https://doi.org/10.2514/1.37878.

[11] Ross, J. C., Heineck, J. T., Halcomb, N., Yamauchi, G. K., Garbeff, T., Burnside, N. J., Kushner, L. K., and Sellers, M. "Comprehensive Study of the Flow around a Simplified Orion Capsule Model." *31st AIAA Applied Aerodynamics Conference*, 2013, pp. 1–17. https://doi.org/10.2514/6.2013-2815.

[12] Murman, S. M., Childs, R. E., and Garcia, J. A. "Simulation of Atmospheric-Entry Capsules in the Subsonic Regime." *53rd AIAA Aerospace Sciences Meeting*, No. January, 2015, pp. 1–21. https://doi.org/10.2514/6.2015-1930.

[13] Bathel, B. F., Borg, S., Jones, S., Overmeyer, A., Walker, E., Goad, W., Clem, M., Schairer, E. T., and Mizukaki, T. "Development of Background-Oriented Schlieren for NASA Langley Research Center Ground Test Facilities." *53rd AIAA Aerospace Sciences Meeting*, No. January, 2015, pp. 1–15. https://doi.org/10.2514/6.2015-1691.

[14] Ivey, C., Danehy, P., Bathel, B., Dyakonov, A., Inman, J., and Jones, S. "Comparison of PLIF and CFD Results for the Orion CEV RCS Jets." No. January, 2011, pp. 1–22. https://doi.org/10.2514/6.2011-713.

[15] Horvath, T. J., Rufer, S. J., and Schuster, D. M. "Infrared Observations of the Orion Capsule During EFT-1 Hypersonic Re-Entry." 2019, pp. 2–23.

[16] Wahls, R. A. "The National Transonic Facility: A Research Retrospective." *39th Aerospace Sciences Meeting and Exhibit*, No. January, 2001. https://doi.org/10.2514/6.2001-754.

[17] Schwing, A. M., and Candler, G. V. "Detached-Eddy Simulation of Capsule Wake Flows and Comparison to Wind-Tunnel Test Data." *Journal of Spacecraft and Rockets*, Vol. 52, No. 2, 2015, pp. 439–449. https://doi.org/10.2514/1.A32834.

[18] Reese, D., Burns, R. A., Danehy, P. M., Walker, E., and Goad, W. *Implementation of a Pulsed-Laser Measurement System in the National Transonic Facility*. AIAA Aviation 2019 Forum, 2019.

[19] Reese, D. T., Thompson, R. J., Burns, R. A., and Danehy, P. M. "Application of Femtosecond-Laser Tagging for Unseeded Velocimetry in a Large-Scale Transonic Cryogenic Wind Tunnel." *Experiments in Fluids*, 2021.

Appendix A: Global Uncertainty

A.1 Absolute and relative spatial uncertainty

In reality, all uncertainties are run specific, but in an effort to provide an estimate of the average global uncertainty value across all the FLEET measurements, the spatial uncertainties were conservatively based on the ability to monitor the beam spot on the floor and the tunnel vibrations. Absolute spatial uncertainty is the uncertainty in the model coordinate system for the overall two-plane sweep and the position of the laser with respect to the model. The relative spatial uncertainty is the uncertainty in physical position from point-to-point within each measurement plane, therefore is only related to the position of the laser itself. These absolute and relative uncertainties are shown in Fig. 19. The values are different for each axis, and as defined the absolute position uncertainty includes the model and laser vibrations and is larger than the relative position uncertainty. The largest uncertainty is in the absolute position

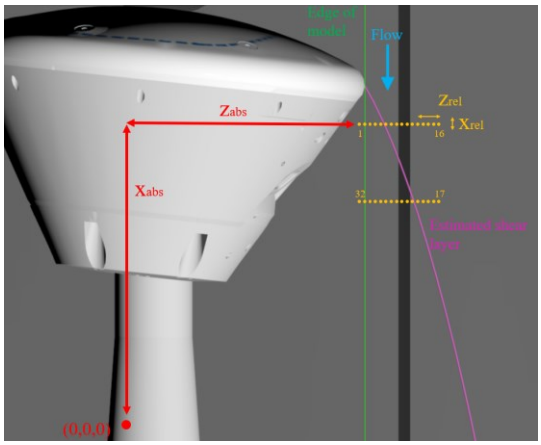

Fig. 19 Visualization of the absolute and relative positions of the measurement planes in the X-Z plane.

of the z-axis, the coordinate near-normal to the imaging plane of the detector. Table 3 lists the spatial uncertainties with the major sources listed as footnotes.

Table 3 Average global uncertainties in the relative and absolute spatial coordinates

	X_{rel}[1]	X_{abs}[2]	Y_{rel}[3]	Y_{abs}[4]	Z_{rel}[5]	Z_{abs}[6]
Spatial Uncertainty (mm)	0.17	1.0	0.17	8.1	0.98	17.0

[1]Uncertainty in the peak of the fitted Gaussian, assumed to be 0.5 pixel for each fit, therefore for a 0.17 mm/pix resolution (worst case, with the detector focused on the model) and a total of 1 pixel the accumulated uncertainty for two measurement points is equal to the resolution, or 0.17 mm.

[2]Typical peak-to-peak oscillation of the model with respect to the beam (6 pixels at 0.17 mm/pix).

[3]Set to one pixel row of the detector at the largest mm/pix detector calibration of 0.17 mm.

[4]Average peak-to-peak value of the model y-oscillations from air runs at M = 0.3, 0.5, and 0.7).

[5]Defined as the standard deviation of all the displacements from point to point in the floor marker monitoring scheme when transformed back to the tunnel centerline.

[6]Assuming the oscillations are similar to the y-axis, the uncertainty is a summation of the y-axis absolute value (8.1 mm) and the uncertainty in the beam center determination from the floor monitoring algorithm, conservatively set to half the radius of the beam spot size on the floor marker (16 pixels on the floor monitoring camera, relating to ~8.9 mm on the tunnel centerline).

A.2 Velocity uncertainty

The global velocity uncertainty in this analysis is limited to the uncertainty in the intensifier gate timing, the spatial calibration of the detector, and the processing of the FLEET lines to determine relative positions of the initial FLEET line and the delayed FLEET line. Uncertainty in the gate timing of the intensifier is assumed to be 50 ns (δt), while the uncertainty in the relative positioning of the FLEET lines is that of the relative x-coordinate uncertainty of 1/10th of a pixel or 17 µm (δx). Therefore, using the standard linear uncertainty propagation formulation from Eq. (1) for a velocity expression of $u = {}^{x}/_{t}$ with relative values of $x = 0.4$ mm and $t = 4$ µs representing a flow velocity of 100 m/s, an estimation of the average global velocity uncertainty is 4.4 m/s, or 4.4%.

$$\delta u = \sqrt{\left(\frac{\partial u}{\partial x}\delta x\right)^2 + \left(\frac{\partial u}{\partial t}\delta t\right)^2} = \sqrt{\left(\frac{1}{t}\delta x\right)^2 + \left(\frac{-x}{t^2}\delta t\right)^2} \qquad (1)$$

This uncertainty propagation expression is plotted in Fig. 20 as a function of tunnel temperature for the three Mach numbers tested to demonstrate trends with the uncertainty with detector delay and the selection of the x-coordinate

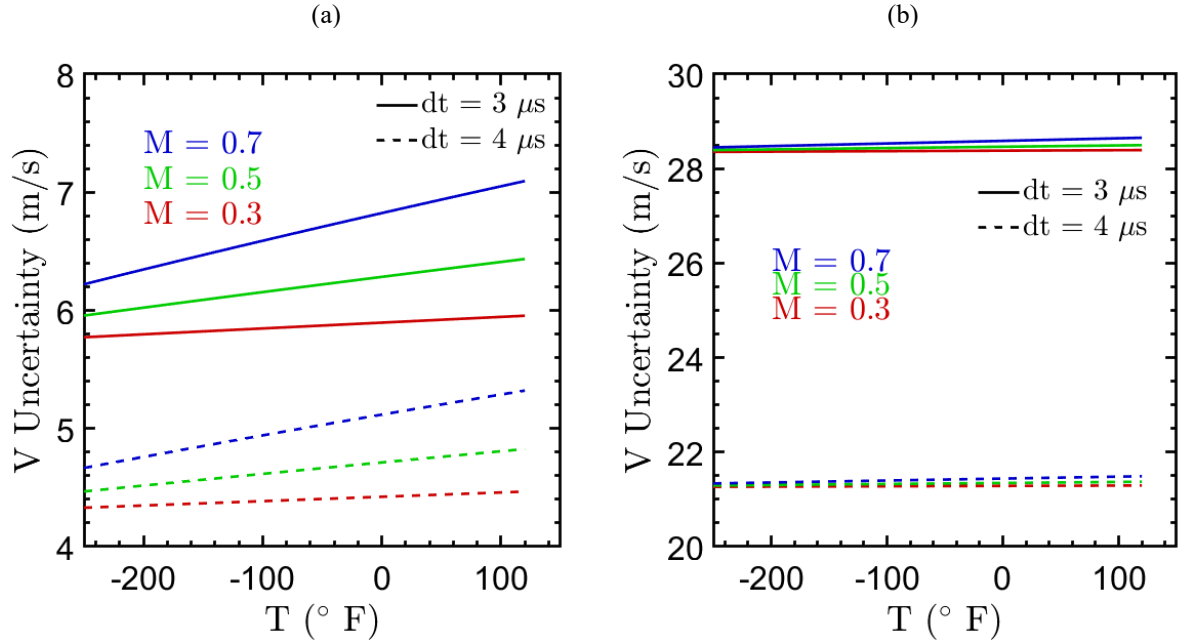

Fig. 20 Velocity uncertainty as a function of gas temperature for Mach numbers of 0.3, 0.5, and 0.7 assuming (a) a x-coordinate uncertainty of 1/10th of a pixel or 17 µm compared to (b) half a pixel or 85 µm.

spatial uncertainty. In general, the shorter the delay, the stronger the FLEET signal but the larger the uncertainty. A 5x increase in the x-coordinate uncertainty leads to a similar ~5x increase in the velocity uncertainty.